Full length article

Impact of surface reflectivity on the ultra-fast laser melting of silicon-germanium alloys

Damiano Ricciarelli [a], Giovanni Mannino [a], Ioannis Deretzis [a], Gaetano Calogero [a],
Giuseppe Fisicaro [a], Richard Daubriac [b], Fuccio Cristiano [b], Remi Demoulin [c],
Paweł P. Michałowski [d], Pablo Acosta-Alba [e], Jean-Michel Hartmann [e], Sébastien Kerdilès [e],
Antonino La Magna [a],*

[a] National Research Council, Institute for Microelectronics and Microsystems (IMM-CNR), VIII Strada 5, Catania, 95121, Italy
[b] The French National Center for Scientific Research, Laboratory for Analysis and Architecture of Systems (LAAS-CNRS) and University of Toulouse, 7av. Du Col. Roche, Toulouse, 31400, France
[c] University of Rouen Normandy, INSA Rouen, CNRS, Group of Physics of Materials, Rouen, 76000, France
[d] Łukasiewicz Research Network—Institute of Microelectronics and Photonics (IMiF), Aleja Lotników 32/46, Warsaw, 02-668, Poland
[e] French Alternative Energies and Atomic Energy Commission, Electronics and Information Technology Laboratory (CEA-LETI), Minatec Campus, Grenoble, F-38054, France

ARTICLE INFO

ABSTRACT

Ultraviolet nanosecond laser annealing (LA) is a powerful tool where strongly confined heating and melting are desirable. In semiconductor technologies the importance of LA increases with the increasing complexity of the proposed integration schemes. Optimizing the LA process along with the experimental design is challenging, especially when complex 3D nanostructured systems with various shapes and phases are involved. Within this context, reliable simulations of laser melting are required for optimizing the process parameters while reducing the number of experimental tests. This gives rise to a virtual Design of Experiments (DoE). $Si_{1-x}Ge_x$ alloys are nowadays used for their compatibility with silicon devices enabling to engineer properties such as strain, carrier mobilities and bandgap. In this work, the laser melting process of relaxed and strained $Si_{1-x}Ge_x$ is simulated with a finite element method/phase field approach. Particularly, we calibrated the dielectric functions of the alloy for its crystalline and liquid phase using experimental data. We highlighted the importance of reproducing the exact reflectivity of the interface between air and the material in its different aggregation states, to correctly mimic the process. We indirectly discovered intriguing features on the optical behaviour of melt silicon-germanium.

1. Introduction

Ultraviolet nanosecond laser annealing (LA) with pulsed power emission (pulse duration below 10^{-6} s) can be integrated in thermal processes for micro- and nano-electronics, yielding versatile and powerful solutions in extremely constrained space and time scales. The heat induced by the laser melts the doped semiconductor substrate. During the subsequent re-crystallization, the dopants move from interstitial sites to substitutional sites, becoming activated, and, further, the rapid solidification of the melt material avoids the formation of disordered or amorphous semiconductors domains. The use of a small wavelength laser results in a melting of well defined regions at the nanoscale with

the advantages of a better control of the involved junctions, avoiding possible damage of neighbouring parts of the device. The dopant atoms redistribute uniformly due to the high diffusivity (10^{-4} cm^2/s in the liquid phase of Si). Moreover, the non-equilibrium segregation during the fast solidification enhances dopant incorporation in the lattice. Thanks to these particular characteristics, laser annealing is nowadays widely used as a post-fabrication annealing technique in microelectronics [1–7].

Optimal control of the process, occurring in a tiny time window of few ns, depending on the laser pulse duration (Δt), is a key challenge

for the successful application of LA. Due to the specificity of the electromagnetic energy absorption and the ultra-rapid thermal diffusion, LA requires a process design which is unique in microelectronics and is complementary to the device design. This complexity impacts the Design of Experiments (DoE) for the optimization of LA processes. Within this context, reliable LA simulations are required to optimize the process parameters while reducing the number of experimental tests [8–11].

Silicon germanium alloys, $Si_{1-x}Ge_x$, have attracted much interest for decades, notably in the microelectronics industry. They are nowadays used in many domains. Indeed, their compatibility with silicon devices enables to engineer properties such as strain, carrier mobilities and bandgap thanks to the higher hole mobility in Ge, smaller band-gap and the relatively small lattice parameter deviation [12–16]. Silicon germanium alloys present peculiar physical properties, for instance the co-presence of Si and Ge in the lattice structure hampers the phononic transport with a consequent U shape of the thermal conductivity vs. alloy fraction coordinate (X) [17–19]. In analogy to pure silicon and germanium, the alloy crystallizes in a diamond-like structure that features semiconductor properties, and it acts as a metal in the liquid phase, with the occurrence of intermediate covalent and metallic bonding frameworks [20].

In this work, we performed XeCl excimer laser melting simulations of silicon-germanium substrates employing a finite element/phase field approach and a custom-built developed software. This solves coupled partial differential equations (PDEs) which rule evolving fields during the pulsed irradiation (e.g., electromagnetic field, temperature, phase, alloy fraction, dopant density, etc.) [8–11]. This computational methodology was previously applied for the laser annealing of silicon and silicon-germanium, limited to strained thin samples with 0.2 Ge content [21]. The calibration of material parameters is fundamental to achieve the full description of the laser melting process, particularly, in previous work, a systematic categorization of the physical parameters, required for the successful simulation of LA processes on $Si_{1-x}Ge_x$, was reported [21]. However, critical issues with respect to the calibration of the dielectric functions of solid and liquid $Si_{1-x}Ge_x$ were also identified, showing a high level of difficulty due to their possible dependencies on the alloy fraction and dopant concentration. The correctness of dielectric functions is crucial to reproduce the air/$Si_{1-x}Ge_x$ interface reflectivity of the sample, which in turns governs the heat transfer from the laser to the specimen [11].

Here, we calibrated the dielectric function of crystalline $Si_{1-x}Ge_x$ at different temperatures, stoichiometries and dopant concentrations by means of spectroscopic ellipsometry. We further fine-tuned the dielectric function of liquid $Si_{1-x}Ge_x$, with an indirect approach, to reproduce the exact melt depth from laser irradiation of relaxed thick samples. The final dielectric function expressions achieved for both crystalline and liquid phase, were validated for the laser annealing simulation of strained thin samples with various Ge content.

Our results show a reasonable agreement between computed and experimental melt depths, confirming that a correct reproduction of the specimen reflectivity, obtained by considering the dielectric functions dependency on alloy fraction and temperature, is key to realistically model the entire laser melting process.

One additional finding from our investigation pertains to the unique reflectivity observed in liquid $Si_{1-x}Ge_x$. We observed that the reflectivity is maximized when the germanium content is at an intermediate level and decreases as the temperature rises. This particular behaviour may arise from the metallic-like character of the liquid and it deserves further investigations.

2. Material and methods

The methodology employed in this paper involves several steps. First, we determined the dielectric functions of both p-doped and undoped crystalline strained $Si_{1-x}Ge_x$ samples. Next, we manufactured

relaxed thick $Si_{1-x}Ge_x$ samples and subjected them to laser annealing. Then, we fine-tuned a custom-built software to realistically simulate laser melting. To this aim, we used experimentally measured values of dielectric functions to calibrate the reflectivity of crystalline $Si_{1-x}Ge_x$ on the software, and we used the melt depths of laser annealed relaxed thick samples to indirectly reproduced the air/liquid $Si_{1-x}Ge_x$ interface reflectivity on the software. Finally, the obtained computational model was tested using previously published datasets of laser annealed strained samples subjected to similar irradiation conditions [21–23]. Details on the technical of all experimental and computational steps follow in the next paragraphs.

2.1. Strained samples manufacture

We fabricated a set of strained $Si_{1-x}Ge_x$ undoped ∼30 nm thick films over a Si substrate (obtained from epitaxial growths below the critical thickness) with 0.1, 0.2, 0.3, and 0.4 Ge alloy fraction, and a set of p-doped (with boron) strained $Si_{1-x}Ge_x$ samples with 0.3 Ge content. The Ge profiles have been measured with Secondary Ions Mass Spectroscopy (SIMS) and the dopant concentrations achieved, C_B, were: $0\,cm^{-3}$ (None), $7.3 \cdot 10^{19}\,cm^{-3}$ (Low), $1.4 \cdot 10^{20}\,cm^{-3}$ (Medium) and $2.3 \cdot 10^{20}\,cm^{-3}$ (High).

2.2. Crystalline $Si_{1-x}Ge_x$ dielectric functions determination

The optical functions of the strained samples mentioned above were quantified by means of spectroscopic ellipsometry. This analysis was performed with a J. A. Woollam VASE ellipsometer. The light source consists of a Xe lamp and a monochromator. Wavelength-by-wavelength measurements were conducted, in equilibrium conditions, at variable temperatures, starting from room temperature, i.e. 298 K, up to 873 K, thanks to an Instec closed chamber with a constant incident flux of N_2. The presence of the monochromator was particularly important, as it enabled optimized measurement steps in specific spectral regions (i.e., a wavelength step of 0.5 nm in the range 300–320 nm, corresponding to a photon energy step of 0.007 eV in the range 4.13–3.87 eV) which are relevant for laser melting processes. A wider step was used elsewhere within the range 1–6 eV.

The dielectric functions were obtained by fitting the experimental data with a dispersion formula based on Tauc–Lorentz oscillators (see Figure S1). For the purpose of this investigation, we consider only dielectric functions values evaluated at 4.02 eV, corresponding to the wavelength of XeCl excimer laser (308 nm).

2.3. Relaxed samples manufacture

Relaxed thick samples were prepared from two 200 mm bulk Si(100) wafers (Czochralski, p-type, 1–50 Ω cm). The whole $Si_{1-x}Ge_x$ layers epitaxy process was performed by reduced pressure chemical vapor deposition (RPCVD) in a Centura 5200C epitaxy chamber. Prior to each $Si_{1-x}Ge_x$ layer epitaxy, a H_2 bake (1373 K, 2 min) was done to remove the native oxide. After the surface cleaning, a graded $Si_{1-x}Ge_x$ buffer layer was grown on each wafer, with specific growth conditions to reach X = 0.2 Ge content for one wafer and X = 0.5 Ge content for the other one, with a 10%/µm ramp (T(X = 0.2) = 1173 K and T(X = 0.5) = 1123 K, P = 20 Torr, precursors: SiH_2Cl_2 + GeH_4). Then, 1.2 µm thick relaxed and undoped $Si_{1-x}Ge_x$ layers were grown with a uniform Ge content of 0.2 and 0.5, corresponding to the Ge content of the buffer layer underneath. Thanks to the high temperature used during the process, the glide of the threading arms of misfit dislocations (i.e. threading dislocations) was enhanced in such way that they remained mostly confined in the graded buffer layers, close to the $Si_{1-x}Ge_x$/Si interface. As a result, the threading dislocations density was significantly reduced in the $Si_{1-x}Ge_x$ top layers (∼ 10^5 cm^2). Following the RPCVD process, the remaining cross-hatch patterns were removed using a two steps (planarization and smoothing) chemical–mechanical polishing (CMP) process thanks to a Mirra CMP system, reducing the thickness of the $Si_{1-x}Ge_x$ top layers from 1.2 µm to ∼ 0.7 µm.

2.4. Laser annealing

Ultraviolet nanosecond laser annealing treatments were performed with a UV laser of type SCREEN-LASSE (LT-3100) with a λ of 308 nm, a pulse duration of 160 ns, 4 Hz repetition rate, < 3% laser beam uniformity and $10 \cdot 10$ mm^2 laser beam. The samples were kept at room temperature and atmospheric pressure, with a constant incident N_2 flux. Single pulse anneals at various energy densities (ED) were carried out, ranging from 0.300 to 2.500 J cm^{-2} with a 0.025 J cm^{-2} incremental step, crossing all main laser regimes, from sub-melt to partial melt of the relaxed Si$_{1-x}$Ge$_x$ layers.

The germanium composition of as-deposited and laser irradiated Si$_{1-x}$Ge$_x$ layers was measured with the Energy Dispersive X-ray spectroscopy (EDX) technique implemented in a high-angle annular dark-field scanning transmission electron microscope (STEM-HAADF) of JEM-ARM200F model. The technique was previously tested and calibrated, see the Supporting Information for more details.

2.5. Laser melting simulations

Numerical simulation of the ultrafast laser melting process, involving solid/liquid phase change, and Ge diffusion phenomena were performed employing a pre-existing finite element method/phase field approach and a custom-built developed code [8,9,11,21]. This tool consists of a Technology Computed-Aided Design (TCAD) package able to simulate the laser annealing process for 1D, 2D and 3D structures [10]. The heat equation, coupled to the time-harmonic solution of Maxwell equations is solved self-consistently including phase and temperature dependency of material parameters, phase change and alloy fraction. The core model equations, more detailed in [8,9,11,21], are provided in (1)–(4).

$$S(r,t) = \frac{\Im(\varepsilon)}{2\rho}|E_{t-h}|^2 \tag{1}$$

$$\rho c_p \frac{\partial T}{\partial t} + [(1-X)L_S + X\Delta L_{S-X}]\frac{\partial h}{\partial t} = \nabla[K\nabla T] + S(r,t) \tag{2}$$

$$\frac{\partial \varphi}{\partial t} = D_\varphi \nabla^2(\varphi) - \frac{\partial F(\varphi,g,h,u)}{\partial \varphi} \tag{3}$$

$$\frac{\partial X}{\partial t} = \nabla[D_X \nabla X] - D_X ln(k)\nabla[M_2 X(1-X)\varphi(1-\varphi)\nabla\varphi] \tag{4}$$

where r is the position, t is the time, φ is the phase (1 for solid and 0 for liquid), T the temperature, X the solute species molar fraction and u the normalized enthalpy respectively. F is the Helmholtz free energy functional, f the Helmholtz free energy density, g and h are related functions chosen to obtain the adequate shape of F in the sharp interface limit. $S(r,t)$ is the heat source due to the laser, $\Im(\varepsilon)$ is the imaginary part of the dielectric function of the material and E_{th} is the time harmonic electric field (from the solution of the corresponding Maxwell equations). L_S is the latent heat of the pure material, ΔL_{S-X} the latent heat change due to the solute, ρ the density, c_p the specific heat, K the thermal conductivity, k the equilibrium segregation coefficient, D_X the solute species diffusivity and M_2 the solute species mobility coefficient.

The interface velocity is evaluated with the following expression from [24]:

$$v(T) = A \cdot exp\left(-\frac{E_a}{k_b T}\right) \cdot \left[1 - exp\left[\left(\frac{\rho L}{k_B N}\right)\left(\frac{1}{T_M} - \frac{1}{T}\right)\right]\right] \tag{5}$$

where A is the velocity prefactor, E_a is the activation energy for the transition of the atoms from the liquid to the solid phase, k_B the Boltzmann constant, N the atomic density, T_M the melting temperature of the material and L is the latent heat.

As shown by Eqs. (1)–(4) the evolving physical fields are the temperature, T, alloy fraction, X and phase field, φ, they clearly depend on space and time and their initial value (t = 0 ns) must be initialized by the user (for all the points of the mesh).
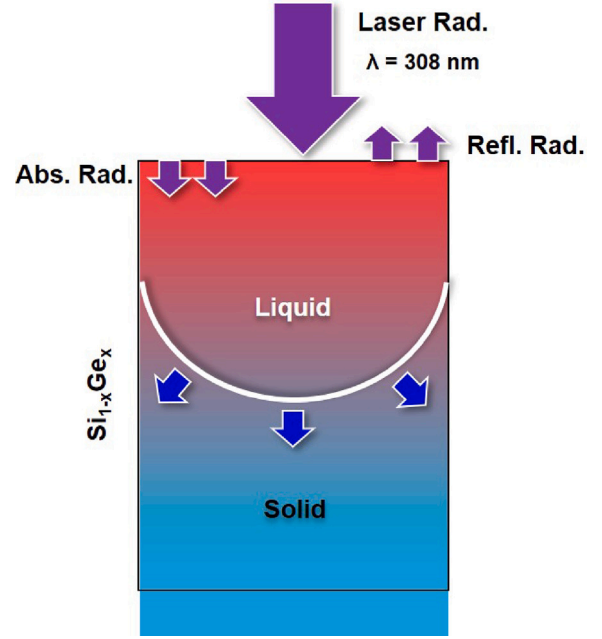

Fig. 1. Schematics of the laser-melting process with laser radiation (Laser Rad.), absorbed radiation (Abs. Rad.) and reflected radiation (Refl. Rad.). Warmer areas are red-coloured, colder ones blue-coloured.

To save computational resources, the phase field model (defined by the above equations) is activated only when $T > T_{melt}$ for a spatial region greater than a user-defined threshold, normally ~8 nm in the mono-dimensional case, while the less costly enthalpy model is used for the other cases [25]. The input CAD geometries and their mesh are built using the gmsh software [26]. The partial derivative equations are solved self-consistently by the FENICS computing platform [27].

With the exception of solid and liquid Si$_{1-x}$Ge$_x$ dielectric functions, calibrated in this work, and of the thermal conductivity, taken from [18], the functions of the material properties involved in the partial derivative equations can be found in [21], where the same custom-built developed software was used.

3. Results and discussion

The laser melting process, as introduced, is sensitive to the fraction of radiation absorbed by the material, i.e the photons not reflected by the surface of the sample. In Fig. 1, we show a simplified scheme of the process. The radiation is partly absorbed by the first few Si$_{1-x}$Ge$_x$ layers and the electromagnetic energy becomes thermal energy. When the alloy reaches the melting temperature, i.e. when the energy density of the laser overcomes a certain ED threshold, the first liquid nuclei start to form. Then, for the duration of the laser pulse Δt, the liquid front covers a distance called melt depth and, eventually, the sample re-crystallizes.

ED thresholds and melt depths are related to the fraction of radiation absorbed, $(1 - R)$, with R being the surface reflectivity. The reflectivity in object is related to the air/Si$_{1-x}$Ge$_x$ interface, as the absorption of the electromagnetic radiation extinguishes within the first nm of the material, i.e. ~5 nm. To accurately simulate laser melting is important to consider the dielectric functions of Si$_{1-x}$Ge$_x$ for crystalline and liquid phases. The first one will mainly determine the melt threshold of the sample, while the second is crucial to obtain the exact melt depth. The link between reflectivity and dielectric function of a certain system at the interface with air is provided by real and complex refractive indices, n and k, through expressions (6)–(8).

$$n = \sqrt{\left[\Re(\varepsilon) + \sqrt{(\Re(\varepsilon))^2 + (\Im(\varepsilon))^2}\right]/2} \tag{6}$$
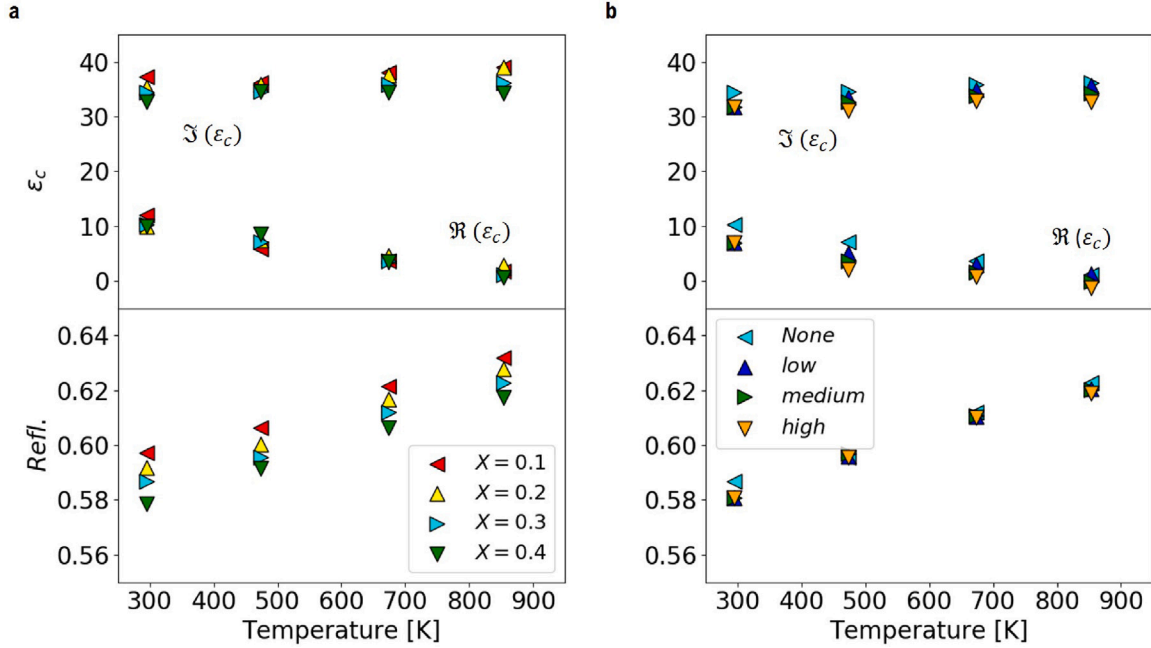
Fig. 2. Imaginary, $\mathfrak{J}(\varepsilon_c)$, real, $\mathfrak{R}(\varepsilon_c)$ parts of dielectric functions values and associated reflectivities measured at 308 nm by spectroscopic ellipsometry at different temperatures and alloy fractions for undoped $Si_{1-x}Ge_x$ (a), and X = 0.3 boron doped $Si_{1-x}Ge_x$ samples (b).

$$k = \mathfrak{J}(\varepsilon)/(2n) \tag{7}$$

$$R = [(n-1)^2 + k^2]/[(n+1)^2 + k^2] \tag{8}$$

We started to determine the dielectric function of crystalline $Si_{1-x}Ge_x$, ε_c, performing a three-dimensional fitting of $\mathfrak{R}(\varepsilon_c)$ and $\mathfrak{J}(\varepsilon_c)$ against temperature (T) and alloy fraction (X). To that end we performed spectroscopic ellipsometry measurements on strained samples, detailed in the methodological section. We considered quantified $\mathfrak{R}(\varepsilon_c)$ and $\mathfrak{J}(\varepsilon_c)$ values corresponding to the XeCl excimer laser wavelength of 308 nm, i.e. 4.02 eV, see Figure S1 for more details on the fitting procedure. The studied alloy fractions were 0.1, 0.2, 0.3 and 0.4, while the temperature range spanned from 295 K to 853 K.

We first inspected the experimental data reported in Fig. 2a as a function of T. $\mathfrak{R}(\varepsilon_c)$ monotonously decreased while $\mathfrak{J}(\varepsilon_c)$ increased with the temperature. This, as shown in the lower part of the panel, resulted in a progressively increased reflectivity with temperature. On the other hand, alloy fraction variations, from 0.1 to 0.4, mainly impacted the imaginary parts, as shown in Fig. 2a, with $\mathfrak{J}(\varepsilon_c(0.1)) > \mathfrak{J}(\varepsilon_c(0.2)) > \mathfrak{J}(\varepsilon_c(0.3)) > \mathfrak{J}(\varepsilon_c(0.4))$. This, turning to reflectivity graphs (lower part of the panel), resulted in a slight decrease of R with the sample alloying.

The effect of p-doping was further assessed for a fixed X = 0.3 alloy fraction. Three boron concentrations, C_B, were evaluated: low $7.3 \cdot 10^{19}$ cm^{-3}, medium $1.4 \cdot 10^{20}$ cm^{-3} and high $2.3 \cdot 10^{20}$ cm^{-3}. The real and imaginary parts of dielectric function at 308 nm, shown in Fig. 2b, presented similar variations in sign and amount, with $\varepsilon_c(low) > \varepsilon_c(medium) > \varepsilon_c(high)$. In terms of reflectivity we found that this results in slight variations among the different doping concentrations, as shown in the bottom of the panel.

The fitting performed is structured on the basis of the following theoretical scheme: $Si_{1-x}Ge_x$ is an almost ideal binary alloy system, where Si and Ge are fully miscible over the whole range of composition. This generally makes the linear interpolation between the physical properties of Si and Ge (using the Ge alloy fraction variable X) a good starting point for the calibration of this material. However, some critical uncertainties exist. A more accurate determination of the dependence of the optical parameters on X in each phase is necessary.

We expressed the real and imaginary parts of the optical dielectric function ε_c as:

$$\varepsilon_c(T, X) = \varepsilon_{c,Ge}(T) \cdot f(X, T) + \varepsilon_{c,Si} \cdot [1 - f(X, T)] \tag{9}$$

where $f(X, T)$ is a monotonically growing polynomial function satisfying the relationships $f(0, T) = 0$ and $f(1, T) = 1$, while $\varepsilon_{c\,Ge}(T)$ and $\varepsilon_{c\,Si}(T)$ are the Ge and Si functions reported in Table 1 from [21]. Only $f(X, T)$ has an unknown form and calibration. We thus considered a second order polynomial function:

$$f(X, T) = a(T) \cdot X^2 + [1 - a(T)] \cdot X \tag{10}$$

In order to determine the temperature dependence of ε_c, the function $a(T)$ was further calibrated as a second-order polynomial:

$$a(T) = b \cdot T^2 + c \cdot T + d \tag{11}$$

A second level of calibration was implemented for p-doped $Si_{1-x}Ge_x$ samples. In this case, the variable C_B was introduced in the ε_c function giving rise to $\varepsilon_c(T, X, C_B)$:

$$\varepsilon_c(T, X, C_B) = \varepsilon_c(T, X) \cdot g(C_B, T) \tag{12}$$

$$g(C_B, T) = 1 - m(T) \cdot C_B/C_0 \tag{13}$$

$$m(T) = b' \cdot T^2 + c' \cdot T + d'. \tag{14}$$

$m(T)$ is a second-order polynomial function of temperature with parameters b', c' and d', while C_0 is a constant yielding $g(C_B, T) \approx 1$ for very low-doping (hence, for very low doping, $\varepsilon_s(T, X, C_B) \approx \varepsilon_s(T, X)$. All fitting parameters were reported in Table 1. We note that the expressions for crystalline Si and Ge were obtained from parameterizations achieved in Ref. Huet et al. [21] by some of us.

Fig. 3a–b shows the calculated reflectivity map (from our fitting expression) for undoped (3a) and boron-doped (Fig. 3b) samples. Coloured dots representing the experimental values were also plotted showing on overall a good agreement between the mathematical model and spectroscopic ellipsometry data. Numerically the errors associated to the modelled reflectivity result within ~5%, as detailed in Table S1 and S2.

A closer look to Fig. 3a highlights a huge dependency of crystal R on the temperature, governed by the material phonons, with a remarkable
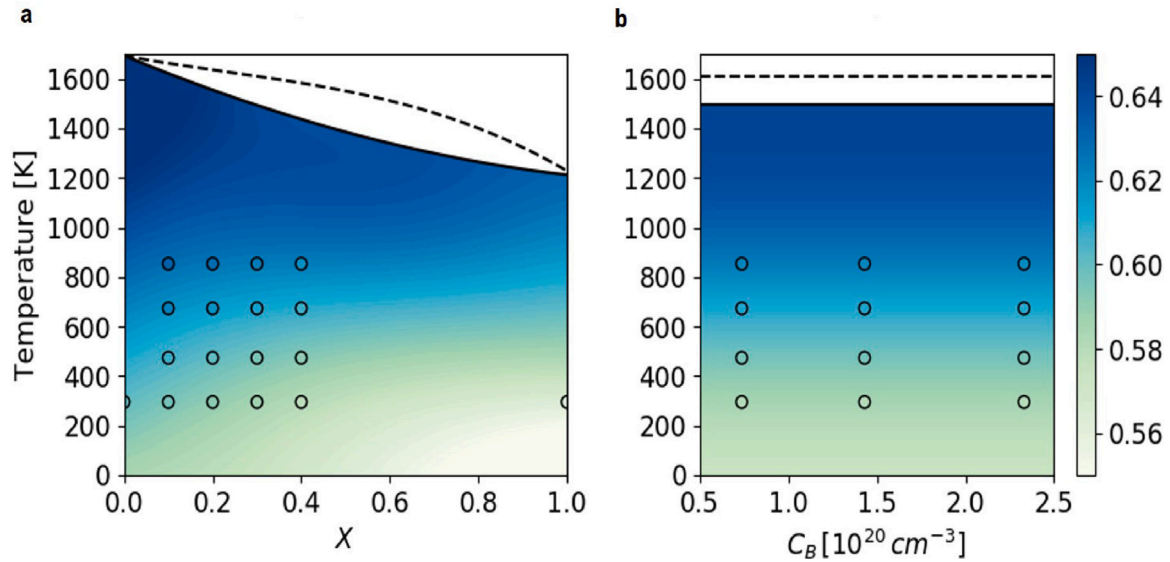
Fig. 3. Reflectivity of $Si_{1-x}Ge_x$ obtained from fitted ε_c for undoped (a) an p-doped X = 0.3 samples (b). The continuous line represents the solidus thermodynamic limit and the dashed one the liquidus, redrawn from [28]. Coloured dots represent the experimental values.

Table 1
List of fitting parameters for the real, $\mathfrak{R}$, and imaginary $\mathfrak{I}$ parts of the dielectric function for doped and undoped crystalline $Si_{1-x}Ge_x$. For definitions cf. main text. Temperature is expressed in K.

	$\mathfrak{R}$	$\mathfrak{I}$
$\varepsilon_{c,Si}$	$(3.912 \cdot 10^{-6}) \cdot T^2 - (1.355 \cdot 10^{-2}) \cdot T + 8.941$	$(-5.225 \cdot 10^{-6}) \cdot T^2 + (1.593 \cdot 10^{-2}) \cdot T + 23.571$
$\varepsilon_{c,Ge}$	$(-9.025 \cdot 10^{-7}) \cdot T^2 - (6.558 \cdot 10^{-3}) \cdot T + 13.892$	$(9.652 \cdot 10^{-3}) \cdot T + 35.069$
b	$2.670 \cdot 10^{-6}$	$6.167 \cdot 10^{-7}$
c	$-8.932 \cdot 10^{-3}$	$-3.678 \cdot 10^{-3}$
d	2.747	0.7241
b'	$-3.043 \cdot 10^{-8}$	$-1.555 \cdot 10^{-9}$
c'	$8.797 \cdot 10^{-5}$	$5.517 \cdot 10^{-7}$
d'	$-4.731 \cdot 10^{-3}$	$4.131 \cdot 10^{-3}$
C_0	$1.001 \cdot 10^{19}$	$1.00 \cdot 10^{19}$

Table 2
Original vs. optimal $\mathfrak{I}(\varepsilon_l)$ values obtained for matching the melt depth at the various laser energy densities. R_l represents liquid reflectivity, T_m the melting point of the alloy and T_l the liquid temperature collected at the interface with air (cf. main text).

		Original $\mathfrak{I}(\varepsilon_l)$				Optimal $\mathfrak{I}(\varepsilon_l)$		
X_l	ED [J/cm^2]	$\mathfrak{I}(\varepsilon_l)$	R_l	T_m [K]	T_l [K]	$\mathfrak{I}(\varepsilon_l)$	R_l	T_l [K]
0.24	0.75	9.98	0.778	1626	1641	7.70	0.811	1640
0.24	0.80	9.98	0.778	1626	1643	6.50	0.833	1641
0.24	1.10	9.98	0.778	1626	1660	8.01	0.806	1652
0.24	1.50	9.98	0.778	1626	1696	9.80	0.780	1693
0.58	0.90	9.77	0.780	1520	1562	7.90	0.803	1557
0.58	1.50	9.77	0.780	1520	1627	10.30	0.768	1630

Table 3
Calibrated parameters for the real and imaginary dielectric functions of liquid $Si_{1-x}Ge_x$. For definitions cf. main text. Temperature is expressed in K.

	$\mathfrak{R}$	$\mathfrak{I}$
$\varepsilon_{l,Si}$	-15.734	10.126
$\varepsilon_{l,Ge}$	-14.585	9.517
b_1	–	0.8787
c_1	–	-496.7
b_2	–	-0.4159
c_2	–	257.9

steepness, while only slight variation can be found when moving along X.

Importantly, we observed that, in the large T and X ranges, the crystalline $Si_{1-x}Ge_x$ reflectivity has an average value of ~0.60.

In the case of p-doped material, Fig. 3b, we observed slight dependence of R on the dopant concentration.

Having obtained a reasonable calibration for the real and imaginary dielectric functions of crystalline $Si_{1-x}Ge_x$, we can now start to use our software to model the laser melting process, however results need to be compared to the experiment. Experimental laser irradiations were performed on relaxed thick samples. The use of relaxed thick samples enabled to evaluate cases where the liquid front covered high distances. A XeCl excimer laser was used, with a wavelength of 308 nm and a laser pulse Δt of 160 ns. Irradiated samples preserved an optimal surface planarity, as shown by Figure S3. The samples exhibited a

constant X alloy fraction of 0.24 and 0.58 for ~ 1200 nm and ~ 3000 nm respectively evaluated by EDX measurements (see Figure S2a–b). These numbers quite differed from the nominal alloy fraction and thickness of the samples, i.e. 0.20 (0.50), and 770 nm (710 nm), due to the local character of the EDX measurements. In the impossibility to perform more sophisticated measurements both for the as-deposited and the irradiated samples, we considered, for modelling purposes, EDX linear interpolated profiles as a reference and we checked the impact of different alloy fraction and thicknesses.

For our computations, we employed a pre-existing code developed by some of us [8,9,11,21] (see related methodological section). The time harmonic electromagnetic field, computed from Maxwell equations, mimicked the one employed experimentally, with a wavelength of 308 nm and a pulse time Δt of 160 ns. We used a simple mono-dimensional mesh with the idea of the scheme in Fig. 4a. The initial alloy fraction profile along Z was taken from the EDX measurements in Figure S2a–b. The mesh presented a total length of 4500 nm (8000 nm) for the case X = 0.24 (X = 0.58) and is divided into three different
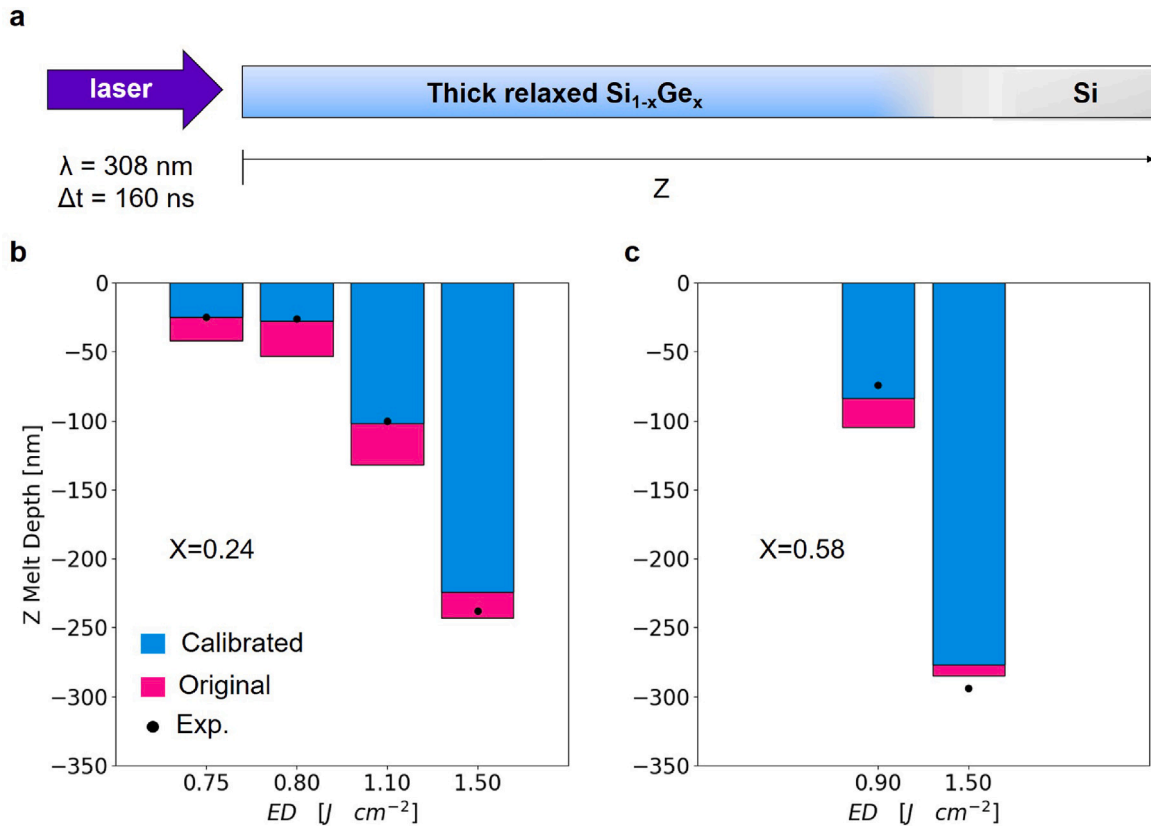
Fig. 4. Schematics of the mono-dimensional model employed for simulating laser annealing on relaxed $Si_{1-x}Ge_x$ samples (a), comparison between experimental and simulated MD for relaxed $Si_{1-x}Ge_x$ samples with initial alloy fractions of 0.24 (b) and 0.58 (c). Cf. main text for definition of calibrated and original models.

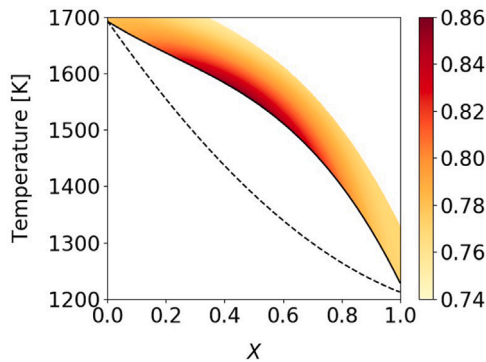**Fig. 5.** Reflectivity map of liquid $Si_{1-x}Ge_x$ at a wavelength of 308 nm as a function of temperature and alloy fraction. The continuous line represents the liquidus and the dashed one the solidus thermodynamic limits, redrawn from [28].

portions with a progressively increased grain: (i) $Si_{1-x}Ge_x$, 1300 nm (3000 nm) long with a constant alloy fraction, (ii) $Si_{1-x}Ge_x$, graded region with a length of 2500 nm (4300 nm) with variable decreasing X and (iii) Si, 700 nm long characterized by X = 0.

The model delivered ED thresholds of 0.55 (0.45) J cm^{-2} for X = 0.24 (X = 0.58) in good agreement with experimental results reported in Table S4. These quite low values, if compared to strained cases [21–23], reflected the thermal properties of thick relaxed samples, where conduction is mainly ascribed to the alloy and not to the Si substrate. Alloying enhances the probability of phonon-phonon scattering events, giving rise to a U shape of the thermal conductivity, with a minimum at X = 0.5. Heat conduction is therefore reduced if compared to pure Si samples with associated drop of ED thresholds [17,18].

In an attempt to evaluate whether or not melting features for laser energy densities > 0.7 J cm^{-2} met experimental findings, see Figure S4 and S5, we firstly approximated the dielectric function of liquid $Si_{1-x}Ge_x$ as a linear combination of $\varepsilon_{l,Si}$ and $\varepsilon_{l,Ge}$ weighted by the respective fractions $(1 - X)$ and X. Real and imaginary dielectric function parts for the elements, were calibrated in previous work [21], and we report them in Table S3.

Unfortunately, this approximation, thereafter called original model, delivered some inconsistency between the simulated melt depths and the experimental ones, as documented in Fig. 4b–c, i.e. comparison between the magenta histograms and the black dots. More specifically, the error bar of computed MDs resulted in more than ~20 nm for smaller EDs, while the agreement was good for higher EDs, as for 1.50 J cm^{-2}. The aforementioned deviations can be explained considering the reflectivity of the melt. As shown in Table 2, our assumption (original model) provided almost identical reflectivity values of the melt, i.e., ~0.78 for all ranges of alloy fractions and temperatures. However, this might not be the case for X far from the two elements. We investigated this aspect, by studying the dependency of the MD on the imaginary dielectric function part. $\Im(\varepsilon_l)$ then became a hyper-parameter that linked the optical constants of $l - Si_{1-x}Ge_x$ to melt depths, enabling an extension of the previous calibration to the liquid phase. We found optimal values of $\Im(\varepsilon_l)$, reported in Table 2 (see Optimal $\Im(\varepsilon_l)$ section), for which obtained MDs overlaps with experiments. These values are associated to specific time-averaged liquid alloy fractions and temperatures, X_l and T_l, reported in Table 2, captured at the air–liquid interface (Z = 0 mesh point). Results collected with this approach (Table 2) underlined an effective dependence of the optical functions on T and X. If we focus on the data for 0.24, we observe that an optimal $l - Si_{1-x}Ge_x$ reflectivity higher than ~0.81 is needed for temperature close the melting point (T_m), while values of ~0.78, similar to those arising from the original model, are required for higher T. The behaviour is identical for X = 0.58.
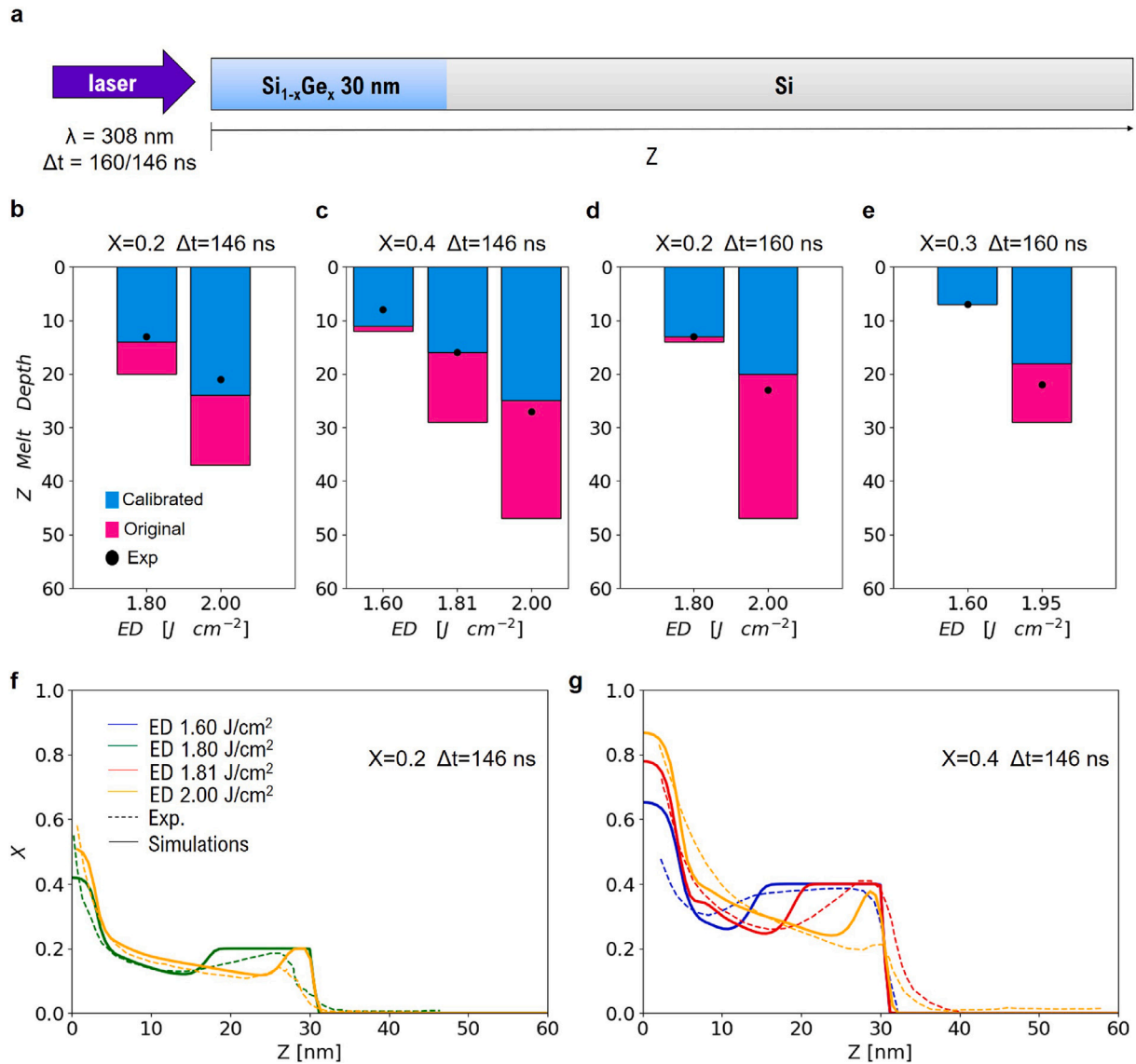
Fig. 6. Schematics of the mono-dimensional model employed for laser annealing simulations on strained $Si_{1-x}Ge_x$ samples (a), comparison between experimental and simulated MDs for a laser pulse of 146 ns (b)(c) and 160 ns (d)(e), experimental vs. simulated germanium profile for X = 0.2 (f) and X = 0.4 (g) with Δt of 146 ns, the experimental profiles are re-drawn from [22,23]. Cf. main text for definitions of original and calibrated models.

Along the same lines than for solid $Si_{1-x}Ge_x$, we elaborated a semi-empirical expression for ε_l, accounting for the specific behaviour of the reflectivity near the melting point, T_m. Due to the limited availability of points, we kept the real part of the function to its original form, i.e. without a temperature dependence, and we varied only its imaginary part. In this framework we had enough degrees of freedom to reproduce the correct reflectivity required to match the experiment.

The $f(X, T)$ function is, at variance with the solid case, cubic on X and linear on T. The cubic dependency on the alloy fraction X was found to be necessary to effectively reproduce, at the same time, the pure elements boundaries X = 0 and X = 1, and the values of the dielectric function at X = 0.24 and X = 0.58. As a matter of fact, previous attempts with a quadratic dependency led to an inexact reproduction of the function at the points used for fitting. The temperature dependency was chosen as linear due to the limited amount of points available. However, we tested a quadratic dependency for X = 0.24 and we found only a marginal impact of higher order T terms in reproducing the experiment (see Table S5). Our semi-empirical expression for $\varepsilon_l(T, X)$ is detailed by (15)–(17).

$$\varepsilon_l(T, X) = \varepsilon_{l-Ge} \cdot f(T, X) + \varepsilon_{l-Si} \cdot [1 - f(T, X)] \tag{15}$$

$$f(X, T) = a_2(T) \cdot X^3 + a_1(T) \cdot X^2 + [1 - a_1(T) - a_2(T)] \cdot X \tag{16}$$

$$a_i(T) = b_i(T - T_{mGe}) + c_i \tag{17}$$

where a_i and b_i are parameters determined by the fitting of the $\Im(\varepsilon_l)$ values in Table 2 vs. X_l and T_l. Temperature was referenced to the lowest melting point of the alloy, corresponding to l-Ge, $T_{m,Ge}$. The obtained b_i and c_i parameters are reported in Table 3 and a reflectivity map for the liquid phase of $Si_{1-x}Ge_x$, is shown in Fig. 5.

The map summarizes two important findings about reflectivity of liquid $Si_{1-x}Ge_x$, (i) a maximum of R on the liquidus line appeared at X = 0.5 and (ii) R monotonously decreases with T. Both effects are ascribed to alloying, highlighting possible alterations of the electronic structure of the liquid not experienced in the crystal, where the R value only slightly differed from the average of 0.60 (Fig. 3a). This deserves further investigations.

We observe that, for similar ED threshold, melt depths of X = 0.58 samples were always deeper than for X = 0.24 because of the smaller melting point.

Table 4

Melt depths obtained for $ED > 2.00$ J cm^{-2} for strained samples with a studied cut-off of the imaginary dielectric function expression. Cf. main text.

X	ED [J cm^{-2}]	Δt [ns]	$\Im(\varepsilon_i)\,cutoff$	$R_l\,cutoff$	MD [nm]	MD exp [nm]
0.2	2.20	146	8.358	0.801	43	38
0.2	2.40	146	8.358	0.801	81	81

The dielectric function calibration, achieved with samples' alloy fraction and thicknesses by EDX measurements, was tested also with the nominal values of the former, as shown in Table S6. As a result of this analysis, we found different thickness of Si$_{1-x}$Ge$_x$ did not alter the melt depths values. Negligible variations were found changing the initial alloy fraction 0.24 to 0.20, while more, though slight, happened when moving from 0.58 to 0.50. Anyway, the error bar was lower than the one arising with the original model of dielectric constants. We performed, for completeness, a calibration considering nominal X as initial Ge concentration (see Table S7).

To validate our fine-tuned model for Si$_{1-x}$Ge$_x$, obtained with data from relaxed samples, we used a pre-existing data-set of strained Si$_{1-x}$Ge$_x$ samples published in [21–23] and fresh measurements performed on samples with X = 0.3 (laser annealing conditions were identical to relaxed samples). These experimental data-set covers germanium contents of 0.20, 0.30 and 0.40. The samples were irradiated with a XeCl laser with pulses Δt of 160 ns and 146 ns.

Modifications to our FEM model, for this validation purpose, embroiled new mesh and initial alloy profile definitions, following the idea of the scheme in Fig. 6a. The mesh was characterized by 30 nm of Si$_{1-x}$Ge$_x$ where the alloy fraction was set as constant followed by 4470 nm of Si. Ultimately, the graded region employed for the relaxed samples was replaced by a sharp Si/Si$_{1-x}$Ge$_x$ interface of ~ 1 nm. The laser pulse was selected as 160 ns or 146 ns, depending on the samples' experimental records.

In line with experiments, we achieved higher ED thresholds (see Table S4) compared to that in relaxed samples, in the range of $1.40 - 1.55$ J cm^{-2}. This is ascribed to the smaller thickness of the samples, implying thermal conduction mainly governed by the silicon buffer.

Turning to melt-depths, our computational results, reported in Fig. 6b–e, confirmed, in all cases, our reflectivity fine-tuning was essential for a correct matching. Accordingly, the cyan histograms are in close agreement with the black dots (experiment), while the magenta bars (original model) are always ~20 nm deeper. The simulated germanium segregation profiles, drawn in Fig. 6f–g along with the experimental ones, featured a good level of accuracy owing to the correct reproduction of the germanium segregation process. Some critical issues occurred as we increased the laser fluency to ED > 2.00 J cm^{-2}. In this regime the liquid front exceeded the 30 nm of strained Si$_{1-x}$Ge$_x$ samples, entering the Si buffer region. Liquid temperatures then reached ~1700 K, a range where our calibration is not trained and yielded an incorrect small reflectivity value of ~0.75. To overcome the limitation (due to temperature expression linearity), we studied a cut-off of the semi-empirical $\Im(\varepsilon_i)$ function yielding R = 0.80 with whom the experiment is matched (Table 4).

4. Conclusions

In conclusion, we showed the importance of correctly reproducing the air/Si$_{1-x}$Ge$_x$ reflectivity of the sample, in the entire ranges of X and T, in order to realistically describe the laser melting process. We addressed the issues related to the Si$_{1-x}$Ge$_x$ dielectric functions calibration, where a better definition of those for the liquid phase was still missing. We fine-tuned the latter with an indirect approach, using relaxed samples' data and we found the resulting model to yield accurate results also when strained samples are considered, achieving reliable

melt depths and alloy redistribution profiles. We described some limitation for cases where the liquid front exceeded the Si$_{1-x}$Ge$_x$/Si interface, whom could anyhow be circumvented with ad-hoc studied cut-offs of the dielectric functions.

Another noteworthy discovery arising from our investigation relates to the distinctive reflectivity exhibited by liquid Si$_{1-x}$Ge$_x$. Our observations indicate that the reflectivity reaches its peak, on the liquidus line, when the germanium content is at an intermediate level, gradually diminishing as the temperature increases. This intriguing trend in reflectivity could be attributed to the liquid's metallic-like properties and it deserves further investigation.

CRediT authorship contribution statement

Damiano Ricciarelli: Conceptualization, Data curation, Investigation, Visualization, Validation, Formal analysis, Writing – original draft. **Giovanni Mannino:** Investigation, Methodology. **Ioannis Deretzis:** Investigation, Data curation, Writing – review & editing. **Gaetano Calogero:** Investigation, Data curation, Writing – review & editing. **Giuseppe Fisicaro:** Investigation, Data curation, Writing – review & editing. **Richard Daubriac:** Investigation, Data curation. **Fuccio Cristiano:** Investigation, Methodology. **Remi Demoulin:** Investigation, Methodology. **Paweł P. Michałowski:** Investigation, Methodology. **Pablo Acosta-Alba:** Investigation, Methodology. **Jean-Michel Hartmann:** Investigation, Methodology. **Sébastien Kerdilès:** Investigation, Methodology. **Antonino La Magna:** Investigation, Methodology, Conceptualization, Formal analysis, Funding acquisition, Project administration, Software, Supervision, Writing – review & editing.

Declaration of competing interest

The authors declare that they have no known competing financial interests or personal relationships that could have appeared to influence the work reported in this paper.

Data availability

No data was used for the research described in the article.

Acknowledgements

Appendix A. Supplementary data

Supplementary material related to this article can be found online at https://doi.org/10.1016/j.mssp.2023.107635.

References

[1] S. Prussin, D.I. Margolese, R.N. Tauber, The nature of defect layer formation for arsenic ion implantation, J. Appl. Phys. 54 (5) (1983) 2316–2326.

[2] P. Baeri, G. Foti, J.M. Poate, S.U. Campisano, A.G. Cullis, Orientation and velocity dependence of solute trapping in Si, Appl. Phys. Lett. 38 (10) (1981) 800–802.

[3] K. Ong, K. Pey, P. Lee, A. Wee, Y. Chong, K. Yeo, X. Wang, Formation of ultra-shallow p^+/n junctions in silicon-on-insulator (SOI) substrate using laser annealing, Mater. Sci. Eng.: B 114–115 (2004) 25–28.

[4] M. Hernandez, J. Venturini, D. Berard, G. Kerrien, T. Sarnet, D. Débarre, J. Boulmer, D. Camel, J.-L. Santailler, H. Akhouayri, Laser thermal processing using an optical coating for ultra shallow junction formation, Mater. Sci. Eng.: B 114–115 (2004) 105–108.

[5] E. Monakhov, B.G. Svensson, M.K. Linnarsson, A. La Magna, M. Italia, V. Privitera, G. Fortunato, M. Cuscunà, L. Mariucci, Boron distribution in silicon after multiple pulse excimer laser annealing, Appl. Phys. Lett. 87 (8) (2005) 081901.

[6] K. Huet, G. Fisicaro, J. Venturini, H. Besaucèle, A. La Magna, Defect kinetics and dopant activation in submicrosecond laser thermal processes, Appl. Phys. Lett. 95 (23) (2009) 231901.

[7] V. Pilipovich, G. Ivlev, Y.F. Morgun, N. Nechaev, V. Osinskii, A.Y. Peshko, Formation of pn junctions in gallium arsenide by laser irradiation, J. Appl. Spectr. 22 (3) (1975) 324–328.

[8] A. La Magna, P. Alippi, V. Privitera, G. Fortunato, M. Camalleri, B. Svensson, A phase-field approach to the simulation of the excimer laser annealing process in Si, J. Appl. Phys. 95 (9) (2004) 4806–4814.

[9] S. Lombardo, S. Boninelli, F. Cristiano, G. Fisicaro, G. Fortunato, M. Grimaldi, G. Impellizzeri, M. Italia, A. Marino, R. Milazzo, E. Napolitani, V. Privitera, A. La Magna, Laser annealing in Si and Ge: Anomalous physical aspects and modeling approaches, Mater. Sci. Semicond. Process. 62 (2017) 80–91.

[10] S. Lombardo, G. Fisicaro, I. Deretzis, A. La Magna, B. Curver, B. Lespinasse, K. Huet, Theoretical study of the laser annealing process in FinFET structures, Appl. Surf. Sci. 467–468 (2019) 666–672.

[11] G. Fisicaro, A. La Magna, Modeling of laser annealing, J. Comp. Electr. 13 (2014) 70–94.

[12] T. Manku, J. McGregor, A. Nathan, D. Roulston, J.-P. Noel, D. Houghton, Drift hole mobility in strained and unstrained doped $Si_{1-x}Ge_x$ alloys, IEEE Trans. Electron Devices 40 (11) (1993) 1990–1996.

[13] S.C. Jain, W. Hayes, Structure, properties and applications of Ge_xSi_{1-x} strained layers and superlattices, Semicond. Sci. Technol. 6 (7) (1991) 547.

[14] S. Iyer, G. Patton, J. Stork, B. Meyerson, D. Harame, Heterojunction bipolar transistors using Si-Ge alloys, IEEE Trans. Electr. Devices 36 (10) (1989) 2043–2064.

[15] R. People, Physics and applications of Ge_xSi_{1-x}/Si strained-layer heterostructures, IEEE J. Quantum Electr. 22 (9) (1986) 1696–1710.

[16] T.P. Pearsall, Silicon-germanium alloys and heterostructures: Optical and electronic properties, Crit. Rev. Solid State Mater. Sci. 15 (6) (1989) 551–600.

[17] P. Maycock, Thermal conductivity of silicon, germanium, III–V compounds and III–V alloys, S. State Electr. 10 (3) (1967) 161–168.

[18] M. Wagner, G. Span, S. Holzer, O. Triebl, T. Grasser, V. Palankovski, Power output improvement of silicon-germanium thermoelectric generators, ECS Trans. 3 (7) (2006) 1151.

[19] T. Hori, T. Shiga, J. Shiomi, Phonon transport analysis of silicon germanium alloys using molecular dynamics simulations, J. Appl. Phys. 113 (20) (2013) 203514.

[20] E. Ko, M. Jain, J.R. Chelikowsky, First principles simulations of SiGe for the liquid and amorphous states, J. Chem. Phys. 117 (7) (2002) 3476–3483.

[21] K. Huet, J. Aubin, P.-E. Raynal, B. Curvers, A. Verstraete, B. Lespinasse, F. Mazzamuto, A. Sciuto, S. Lombardo, A. La Magna, P. Acosta-Alba, L. Dagault, C. Licitra, J.-M. Hartmann, S. Kerdilès, Pulsed laser annealing for advanced technology nodes: Modeling and calibration, Appl. Surf. Sci. 505 (2020) 144470.

[22] L. Dagault, P. Acosta-Alba, S. Kerdilès, J.P. Barnes, J.M. Hartmann, P. Gergaud, T.T. Nguyen, A. Grenier, A.M. Papon, N. Bernier, V. Delaye, J. Aubin, F. Cristiano, Impact of UV nanosecond laser annealing on composition and strain of undoped $Si_{0.8}Ge_{0.2}$ epitaxial layers, ECS J. Solid State Sci. Technol. 8 (2019) 202–208.

[23] L. Dagault, S. Kerdilès, P. Acosta Alba, J.-M. Hartmann, J.-P. Barnes, P. Gergaud, E. Scheid, F. Cristiano, Investigation of recrystallization and stress relaxation in nanosecond laser annealed $Si_{1-x}Ge_x/Si$ epilayers, Appl. Surf. Sci. 527 (2020) 146752.

[24] A. Mittiga, L. Fornarini, R. Carluccio, Numerical modeling of laser induced phase transitions in silicon, Appl. Surf. Sci. 154–155 (2000) 112–117.

[25] S.F. Lombardo, I. Deretzis, A. Sciuto, A. La Magna, Chapter 6 - continuum modeling and TCAD simulations of laser-related phenomena in CMOS applications, in: F. Cristiano, A. La Magna (Eds.), Laser Annealing Processes in Semiconductor Technology, in: Woodhead Publishing Series in Electronic and Optical Materials, Woodhead Publishing, 2021, pp. 251–291.

[26] C. Geuzaine, J.-F. Remacle, Gmsh: A 3-D finite element mesh generator with built-in pre- and post-processing facilities, Int. J. Numer. Methods Eng. 79 (11) (2009) 1309–1331.

[27] M. Alnæs, J. Blechta, J. Hake, A. Johansson, B. Kehlet, A. Logg, C. Richardson, J. Ring, M. Rognes, G.N. Wells, The FEniCS project version 1.5, Arch. Numer. Softw. 3 (100) (2015).

[28] R.W. Olesinski, G.J. Abbaschian, The Ge-Si (germanium-silicon) system, Bull. Alloy Phase Diagrams 5 (2) (1984) 180–183.